Chemical Science

EDGE ARTICLE

View Article Online
View Journal | View Issue

Cite this: *Chem. Sci.*, 2016, **7**, 5922

Study of double core hole excitations in molecules by X-ray double-quantum-coherence signals: a multi-configuration simulation†

Weijie Hua,[ab] Kochise Bennett,[a] Yu Zhang,[a] Yi Luo[bc] and Shaul Mukamel*[a]

Received 9th April 2016
Accepted 11th May 2016

DOI: 10.1039/c6sc01571a

www.rsc.org/chemicalscience

The multi-configurational self-consistent field method is employed to simulate the two-dimensional all-X-ray double-quantum-coherence (XDQC) spectroscopy, a four-wave mixing signal that provides direct signatures of double core hole (DCH) states. The valence electronic structure is probed by capturing the correlation between the single (SCH) and double core hole states. The state-averaged restricted-active-space self-consistent field (SA-RASSCF) approach is used which can treat the valence, SCH, and DCH states at the same theoretical level, and applies to all types of DCHs (located on one or two atoms, K-edge or L-edge), with both accuracy and efficiency. Orbital relaxation introduced by the core hole(s) and the static electron correlation is properly accounted for. The XDQC process can take place *via* different intermediate DCH state channels by tuning the pulse frequencies. We simulate the XDQC signals for the three isomers of aminophenol at 8 pulse frequency configurations, covering all DCH pathways involving the N1s and O1s core hole (N1sN1s, O1sO1s and N1sO1s), which reveal different patterns of valence excitations.

Introduction

X-ray spectroscopies of core level electronic excitations serve as efficient tools in characterizing chemical and electronic structures, thanks to their element selectivity and high sensitivity.[1] With recent development of X-ray laser technology, bright and ultrashort pulses can be generated by the X-ray free electron laser (XFEL)[2] and high harmonic generation (HHG) tabletop[3] sources. This opens up all-X-ray nonlinear spectroscopy which provides higher level of information compared to linear absorption and emission. Various nonlinear X-ray spectroscopies have been proposed and realized experimentally.[4–11] All-X-ray four-wave-mixing (FWM) signals require high intensity light sources. Very recently, FEL-based FWM experimental setup at the extreme ultraviolet (EUV) and soft X-ray regions has been reported,[12] and signals stimulated by EUV transient gratings had been measured.[13]

Two-dimensional (2D) X-ray double-quantum-coherence (XDQC) is a promising FWM technique.[5,14,15] Sequences of pulses are used to probe the valence structure by capturing the correlation between single (SCH) and double core hole (DCH) *excited* states [note that here SCH/DCH denote excited states of neutral molecules rather than SCH/DCH *ionized* states (*i.e.*, cations)]. The signal is generated in the $\mathbf{k}_{III} = \mathbf{k}_1 + \mathbf{k}_2 - \mathbf{k}_3$ direction, with $\mathbf{k}_1$, $\mathbf{k}_2$, and $\mathbf{k}_3$ the wave vectors of the three incident pulses in chronological order. This technique was originally developed in NMR and has been successfully applied to elucidate the coupling of two nuclei. It was then extended to the infrared and visible regimes.[16] Theoretical studies on the X-ray analogue are thus required to explore its potential and performance, help interpret the signals and understand the underlying chemistry.

Double vacancies in core orbitals were studied theoretically by Cederbaum *et al.*[18,19] in the 1980s and the extreme sensitivity of chemical shifts of the DCH ionized states was found. In recent years, inner-shell double photo-ionization attracted much attention by researchers. Experiments were performed for inert gases[20–22] and small molecules [CO, CO_2, N_2, N_2O, H_2O, NH_3, CH_4, C_6H_6, C_2H_{2n} ($n = 1$–3), H_2S, SO_2, CS_2, aminophenols, *etc.*] in the gas phase based on third-generation synchrotron and newly developed XFEL light sources,[23–36] see ref. 37 and 38 for recent reviews. A double core-hole in a molecule can reside on the same atom (single-site or 1-site DCH) or on two different atoms (two-site or 2-site DCH). The double core vacancy can be generated by sequential absorption of two X-ray photons or simultaneously by one photon. With EUV or hard X-ray FEL lasers, multiple X-ray ionization atoms can be prepared and highly charged Xe and fully-stripped Ne cations were observed.[20,21] Instead of ionization to continuum, one or two of

[a]Department of Chemistry, University of California, Irvine, CA 92697-2025, USA. E-mail: smukamel@uci.edu

[b]Department of Theoretical Chemistry and Biology, School of Biotechnology, KTH Royal Institute of Technology, S-10691 Stockholm, Sweden

[c]Hefei National Laboratory for Physical Sciences at the Microscale, University of Science and Technology of China, Hefei, Anhui 230026, China

† Electronic supplementary information (ESI) available: Simulated XANES spectra with better resolved continuum region; RASSCF energy levels of *p*-aminopheol; XDQC signals *via* diagram-A pathway. See DOI: 10.1039/c6sc01571a

the K-shell core electrons can also be excited to the unoccupied molecular orbitals.[23,30,31,33,39] DCH excitations of 1s2s or 1s2p core electrons to unoccupied levels had been observed in SiX_4 (X = H, F, Cl, Br, CH_3) molecules.[40] Extensive simulations on molecular DCH states were carried out mainly using the restricted-active-space self-consistent field (RASSCF) method[23,27,28,35,41,42] and the many-body Green's function based algebraic diagrammatic construction (ADC) method truncated at different orders.[18,26,43] Other approaches include the density functional theory (DFT),[5,26,32,34] time-dependent DFT (TDDFT),[15] second-order Møller–Plesset (MP2),[25] MP4SDQ,[44] Configuration Interaction with singles and doubles (CISD),[33] and multi-reference CI (MRCI)[26] methods. Methods for core hole states and X-ray spectra such as DCH states are reviewed in ref. 8.

The experimental setup for XDQC signal is schematically shown in Fig. 1. We use g, e/e′, and f to denote the ground, SCH, and DCH states, respectively. The ground state energy is set as 0. The two contributing terms to this signal are given by loop diagrams shown in Fig. 1c. During the interaction with the first two pulses $\mathbf{k}_1$ and $\mathbf{k}_2$, the molecular density matrix is promoted from the ground state population to the ground–SCH coherence, and then to the ground–DCH coherence, *i.e.*, $\rho_{gg} \mapsto \rho_{eg} \mapsto \rho_{fg}$. This holds the same for both diagrams. The third pulse $\mathbf{k}_3$ then sets the system to be in $\rho_{e'g}$ or $\rho_{fe'}$ coherence (diagrams A and B respectively) during the final propagation time. Making the rotating wave approximation (RWA)[45] for all interactions between the electromagnetic field and molecule, the field frequency and molecule excitation frequency have opposite signs (expressions for signals are given in the Appendix). Thus, by tuning the central carrier frequencies of the four pulses ω_1–ω_4 to match the ground–SCH or SCH–DCH transitions energies, various excitations are probed as resonances in XDQC signals.

The challenge of XDQC signal simulations lies in computing valence, SCH and DCH excited states with both accuracy and efficiency, and the corresponding transition dipole moments (TDMs) for valence–SCH and SCH–DCH state pairs.[8] Previous signal calculations[5,15] only considered the 2-site DCH states at the DFT level. The earlier work[5] treated the two core holes by using the equivalent core hole (ECH) approximation (also known as the $Z + 1$ approximation).[46] Within this approximation, the core excited atom is replaced by the next element in the periodic table while the number of electrons remains unchanged. This approximation can adequately describe deep 1s core excited states, in good agreement with experimental K-edge X-ray absorption spectra [XAS, *i.e.*, X-ray absorption near edge structure (XANES) or near-edge X-ray fine-structure (NEXAFS)] of various large molecules and materials (see ref. 47 and references therein). When both core holes are treated by the ECH approximation, calculation of DCH states is turned into a ground-state-like, single-determinant problem of the dication.[5] This holds the simplest level of theory to describe DCH-related signals and is limited only for 2-site DCHs on the 1s orbitals. The ECH approximation had been combined with the linear-response TDDFT to model molecules with both a core and a valence holes, and to calculate the shake-up satellites in K-edge X-ray photoelectron spectra.[48] We recently[15] developed

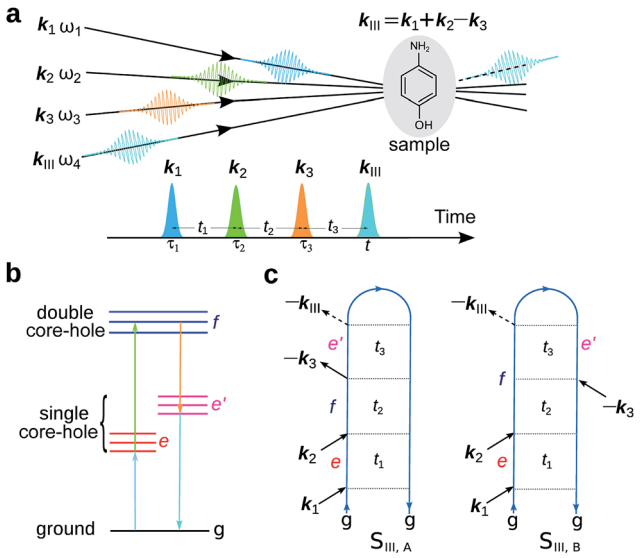

Fig. 1 Setup for the X-ray double-quantum-coherence signal measurement. (a) Pulse sequence. (b) Molecular energy level scheme. g, e/e′, and f denote the ground, single, and double core-hole states, respectively. For instance, when f is a N1sO1s DCH state, e/e′ can be either a N1s or O1s SCH state; when f is a N1sN1s DCH state, e/e′ refers to a N1s SCH state. (c) Two contributing loop diagrams. Both diagrams show a wavefunction evolution pathway of g → e → f → e′ → g (see ref. 17 for diagram rules).

a new scheme to model the DCH states, where one of the two excited atoms is treated by the excited core hole (XCH) approximation,[49] and based on this XCH reference state (Kohn–Sham single determinant) the other core hole is considered by linear response (TDDFT with restricted excitation window).[50] Since unrestricted reference is used, spin contaminated states over a threshold are omitted after the calculations.[51] This method treats orbital relaxation and electronic correlations better than the ECH approximation and is still practical for relatively large systems. However, treating two core holes at different levels introduces nonphysical bias as there are two possibilities in assigning the two levels. Intuitively, both core holes can be explicitly considered within this TDDFT framework. But a double core hole within a single-determinant may easily lead to SCF convergence problems and the collapse of the wavefunction to a low-energy state. More practical method is necessary to better describe double core holes.

In this work we employ the state-averaged RASSCF (SA-RASSCF) method[52] for XDQC signal simulations. Within this multi-configurational approach, the two core holes (whether single or two site) are explicitly treated at the same theoretical level. Multiple configurations better describe the static electron correlation. The core hole can reside in any inner shells including the 1s levels. Using RASSCF to calculate core-excited states dated back to the 1980s study of Ågren and coworkers,[41,53] where state-specific RASSCF was used for the lowest SCH and DCH states, and correlation and relaxation effects on energies were systematically analyzed. In recent years, Tashiro *et al.*[23,42] had employed the method to calculate double ionized states and spectra of various small molecules. Calculating a manifold

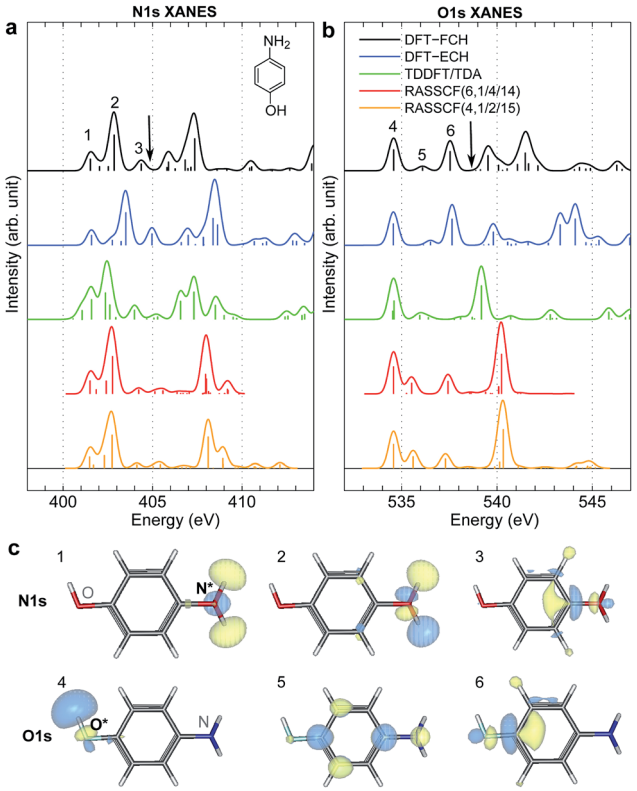

Fig. 2 (a) N1s and (b) O1s XANES spectra of *p*-aminophenol simulated by different methods. Arrows mark the calculated IPs (404.9 and 538.5 eV) by the DFT-FCH method. Major peaks below IP are labeled. The DFT-FCH energies have been shifted using the ΔKohn-Sham scheme[61] and scalar relativistic corrections;[62] other methods were then calibrated to it by aligning the first resolved peak. Shifts applied: DFT-FCH (−5.7 and −6.7 eV for N1s and O1s spectra), DFT-ECH (−123.1, −141.2 eV), TDDFT/TDA (11.7, 13.7 eV), RASSCF (6, 1/4/14) (−3.9, −3.9 eV), RASSCF (4, 1/2/15) (−4.9, −5.1 eV). (c) DFT-ECH final-state molecular orbitals for each peak (contour isovalue = 0.08). Core excited nitrogen and oxygen are labeled by N* and O*.

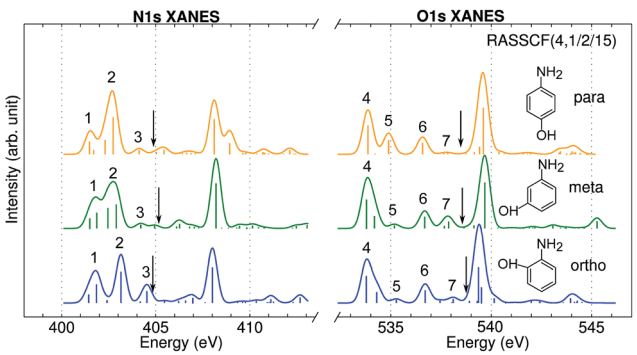

Fig. 3 N1s and O1s XANES spectra of *p*-, *m*-, *o*-aminophenols calculated at the RASSCF (4, 1/2/15) level. Arrows mark the calculated IP by the DFT-FCH method: 404.9, 405.1, 404.8 eV (N1s edge); 538.5, 538.7, 538.8 eV (O1s edge). Major peaks below IP are labeled.

of core excited states requires state-averaging. The SA-RASSCF method[52] has been used to calculate a series of valence and SCH states for spectroscopy use. Odelius and coworkers[54] had

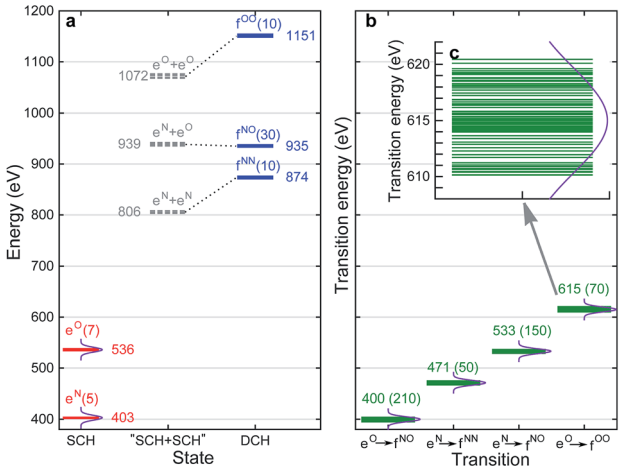

Fig. 4 (a) RASSCF energy levels for *p*-aminophenol. The ground state energy is taken as 0. e^N and e^O are N1s and O1s single core hole states, respectively, f^{NN}, f^{NO}, f^{OO} are N1sN1s, N1sO1s, O1sO1s double core hole states. The number of states or transitions is given in parentheses, and the middle energy of each manifold is given for each band. Gray dashed lines are "DCH states" constructed from summation of corresponding SCH states (*i.e.*, without relaxation). Dotted lines are to show the relaxation effects. (b) SCH–DCH transition energies. Middle value of each band is given, and the number of transitions is given in parentheses. Violet curves denote the power spectrum of Gaussian pulse used in XDQC signal calculations with fwhm = 10.96 eV (corresponding to $\sigma_j = 100$ as), centering at the band average energies. (c) O1s to O1sO1s transitions in panel (b) on an expanded scale.

Table 1 Central carrier frequencies of four pulses (in eV) at each labeled pulse configuration which dominates the diagram-A pathway. Swapping ω_3 and ω_4 (while keeping ω_1 and ω_2) activates the diagram-B pathway, and the pulse configurations are then denoted as ON-B, NO-B, NN-B, OO-B

Pulse configuration[a,b]	ω_1	ω_2	ω_3	ω_4
ON-A	536	400	533	403
NO-A	403	533	400	536
NN-A	403	471	471	403
OO-A	536	615	615	536

[a] *E.g.*, ON means that the molecule is excited to O1s SCH states by ω_1 first, and then to O1sN1s DCH states by ω_2. [b] A (or B) denotes whether the dominant pathway in Fig. 1 is diagram A or B.

employed RASSCF and second-order perturbation theory restricted active space (RASPT2) for L-edge XANES and resonant inelastic X-ray scattering (RIXS) spectra of transitional-metal based complexes, computations were performed for other various similar systems.[11,55] Cost and sensitivity of this method have been carefully investigated.[56] Hua *et al.*[57] employed SA-RASSCF to calculate core-excited states of conical intersection structures and time-resolved stimulated X-ray Raman signals during the photo-induced furan ring-opening reaction pathway. The RASSCF method is commonly viewed as the basis for more accurate multi-configurational electron correlation methods. More accurate signals can be expected by extension, for example, using the RASPT2 method.[58]

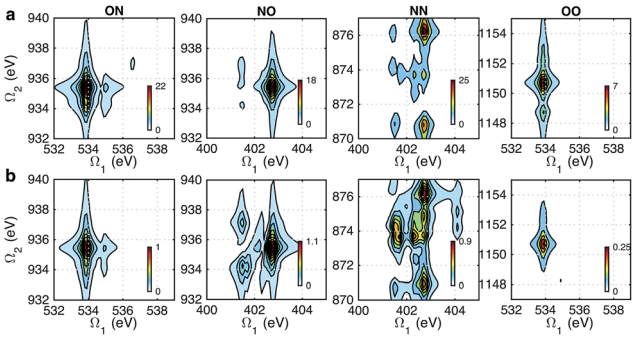

Fig. 5 XDQC signals $S_{III}(t_3 = 6.1$ fs, Ω_2, $\Omega_1)$ (absolute values) of *p*-aminophenol for 8 pulse configurations calculated at the RASSCF level. ON, NO, NN, and OO are selected by tuning pulse frequencies ω_1 and ω_2. ON and NO pulse configurations create two-site N1sO1s DCH states (generated *via* O1s and N1s SCH excited states, respectively); NN and OO generate one-site N1sN1s and O1sO1s DCH states, respectively. Different ω_3 and ω_4 frequency settings select either (a) diagram A or (b) diagram B (see diagrams in Fig. 1c). Both diagrams do not contribute to the same signal for our parameter regime. All pulses have duration of $\sigma = 100$ as.

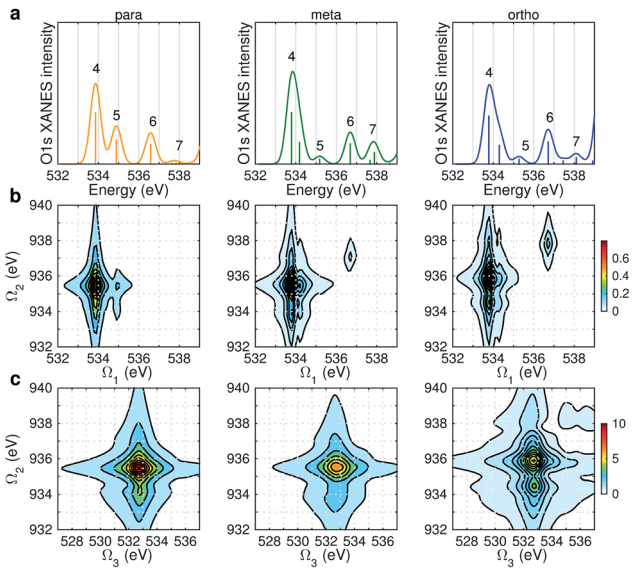

Fig. 6 (a) Simulated O1s XANES spectra of *p*-, *m*-, and *o*-aminophenols (left to right) from Fig. 3. (b–c) ON-B XDQC signals (absolute values) (see Table 1 for notation): (b) $S_{III}(t_3 = 6.1$ fs, Ω_2, $\Omega_1)$, (c) $S_{III}(\Omega_3$, Ω_2, $t_1 = 0$ fs).

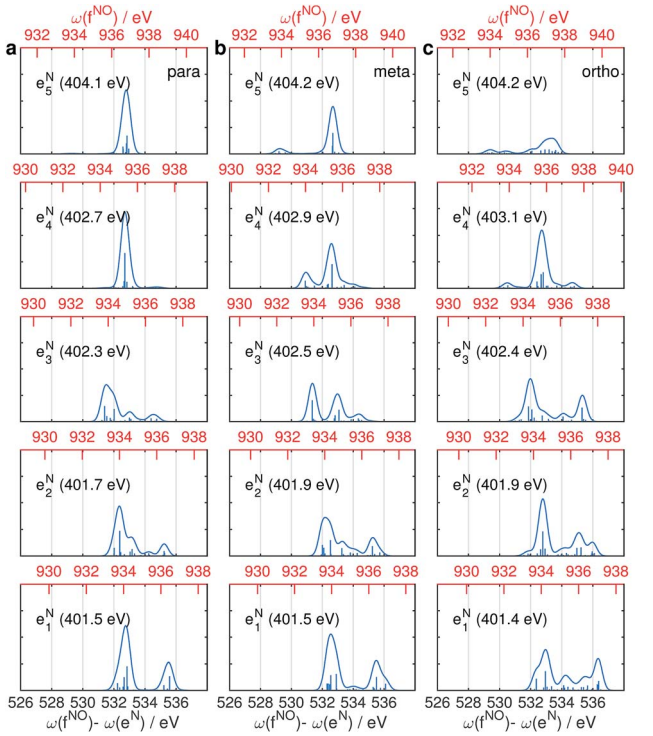

Fig. 7 Oscillator strengths between the lowest 5 N1s excited SCH states (e_i^N) and the lowest 30 N1sO1s DCH states (f_j^{NO}) for *p*-, *m*-, and *o*-aminophenols (a–c). Transition energies are given in bottom *x*-axis (in black) and energies of the DCH states are given in top *x*-axis (in red). Energy of each N1s state is marked in each panel.

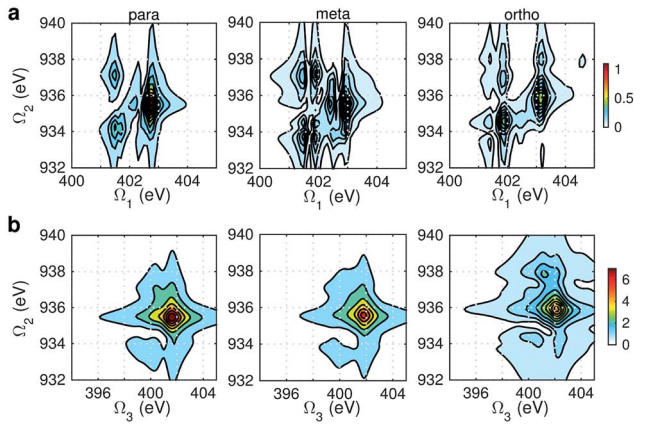

Fig. 8 NO–B XDQC signals (absolute values) of *p*-, *m*-, and *o*-aminophenols (left to right). (a) $S_{III}(t_3 = 6.1$ fs, Ω_2, $\Omega_1)$, (b) $S_{III}(\Omega_3$, Ω_2, $t_1 = 0$ fs).

We study the double core excitations of three isomers of aminophenols by XDQC signals simulated at the RASSCF level. These molecules have two strong electron-donating groups $-NH_2$ and –OH bonded to benzene, at the *para*-, *meta*-, and *ortho*- (abbreviated as *p*-, *m*-, *o*- respectively) positions (also known as 4-, 3-, and 2-aminophenol, respectively). Aminophenols are important electrochemical materials used in dye industry,[59] and the *para* isomer is used as a π-donor in charge transfer complexes.[60] These molecules serve as simple models to demonstrate the multidimensional nonlinear X-ray signals involving double core holes[4] and were employed in DCH ionization studies.[26,34] We examine and compare the spectra of these isomers *via* different DCH pathways selected by varying the pulse frequencies. All possible DCHs created on the 1s orbitals of nitrogen and/or oxygen are considered, including 1-site DCHs on nitrogen (N1sN1s) or oxygen (O1sO1s) and 2-site DCHs on both atoms (N1sO1s).

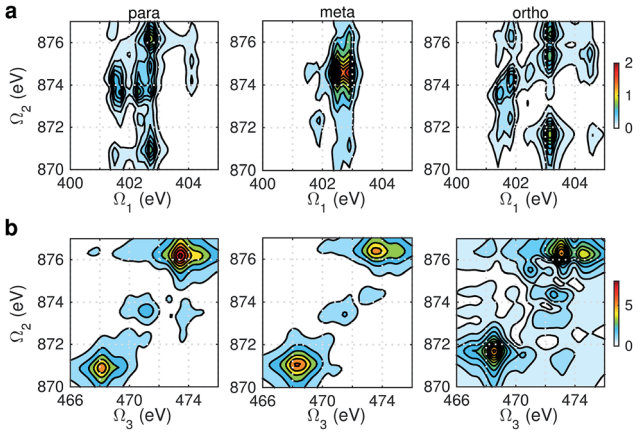

Fig. 9 NN-B XDQC signals (absolute values) of *p*-, *m*-, and *o*-aminophenols (left to right). (a) $S_{III}(t_3 = 6.1$ fs, Ω_2, $\Omega_1)$, (b) $S_{III}(\Omega_3$, Ω_2, $t_1 = 0$ fs).

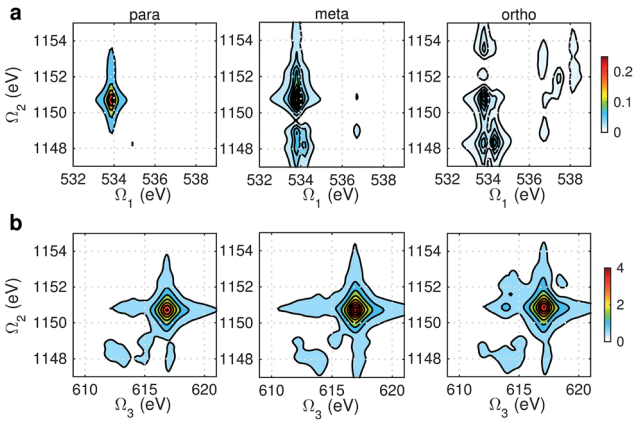

Fig. 10 OO-B XDQC signals (absolute values) of *p*-, *m*-, and *o*-aminophenols (left to right). (a) $S_{III}(t_3 = 6.1$ fs, Ω_2, $\Omega_1)$, (b) $S_{III}(\Omega_3$, Ω_2, $t_1 = 0$ fs).

Results and discussion

XANES

XANES spectra serve as a guide to set up the pulse parameters in XDQC, and provide a window to estimate the accuracy of the simulated XDQC signals. To calibrate our method, we also calculate the XANES spectra at the N1s and O1s edges by RASSCF with different active spaces, and compare it with various DFT methods. Two RASSCF active spaces were (6, 1/4/14) and (4, 1/2/15), where the numbers in parentheses refer to the number of electrons, and numbers of active orbitals in the RAS1, RAS2, and RAS3 space, respectively. The DFT methods include static DFT with the full core hole (FCH) and ECH approximations, and TDDFT with the Tamm–Dancoff approximation (TDA),[63] all using the B3LYP functional.[64] Fig. 2 compares N1s and O1s XANES spectra of *p*-aminophenol simulated by different methods. Results show good agreement between RASSCF and DFT, which are not sensitive to the variation of the active space. Three main features appear below the ionic potentials (IP) in both edges. In Fig. 2a, the pre-shoulder

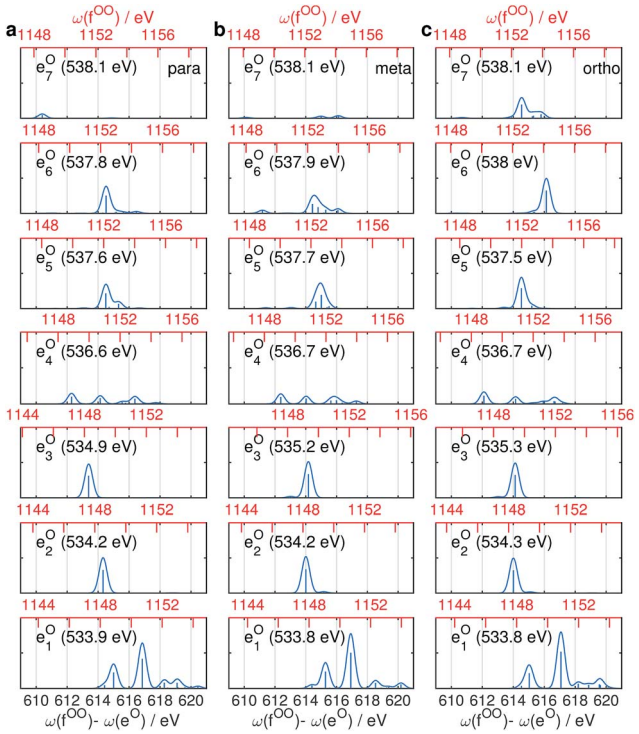

Fig. 11 Oscillator strengths between the lowest 7 O1s excited SCH states (e_i^O) and the lowest 10 O1sO1s DCH states (f_j^{OO}) for *p*-, *m*-, and *o*-aminophenols (a–c). Transition energies are given in bottom *x*-axis (in black) and energies of the DCH states are given in top *x*-axis (in red). Energy of each O1s state is marked in each panel.

peak 1 (401.6 eV) comes from the N1s → σ^*_{N-H} transitions (see orbitals in Fig. 2c). The strong peak 2 is dominated by transitions of the same type, with also contributions from the N1s → π* resonance. The separation to peak 1 differs from these approaches (in ascending order): 0.8 eV by TDDFT/TDA, 1.1 eV by the two RASSCF methods, 1.2 eV by DFT-FCH and 1.9 eV by DFT-ECH. A weak peak 3 appears at 404–405 eV, originating from the N1s → σ^*_{N-C} transition. In Fig. 2b, peaks 4, 5, 6 are assigned as O1s → σ^*_{O-H}, O1s → π*, and O1s → σ^*_{O-C} transitions, respectively. All methods give the three peaks with similar relative positions and intensities, except that peak 6 almost vanishes in TDDFT/TDA. Comparison of different levels verifies the accuracy of our RASSCF approach. To our knowledge no experimental XANES spectra of this molecule are available. The theoretical spectra [calibrated according to the ΔKohn–Sham (ΔKS) scheme[61]] are estimated to have ~1–2 eV accuracy in absolute excitation energies according to our experience (for comparison of light-element K-edge XANES spectra predicted by this procedure to experiment, see, *e.g.*, ref. 65). Our computed IPs (404.9 and 538.5 eV) compare well with previous theoretical (404.9 and 538.3 eV)[26] and experimental (405.4 and 539.2 eV)[34] results. Note that this work focuses on bound states (region below IP), and we used constant small hwhm in spectral broadening for better comparison of different methods. To better resolve the continuum region, a different convolution scheme[66] with larger hwhm above the IP was employed and given in Fig. S1.†

Fig. 3 shows the calculated N1s and O1s XANES spectra of the three aminophenol isomers at the RASSCF (4, 1/2/15) level. The spectra are very similar and show 3 main features below the IPs in both the N and O K-edges. Peak positions differ by less than 0.4 eV. Peak 3 and 5 intensities also show notable differences: peak 3 is the strongest for *o*-aminophenol, and peak 5 is the strongest for *p*-aminophenol. These fine details could be observed by high-resolution measurements.

Selection of states and pulse parameters

With XANES at hand, only bound SCH states (sticks up till the IPs) were considered in XDQC signal simulations, which only include several states of 3–5 eVs. We selected DCH states such that the SCH–DCH transition energies are within a 10 eV window. Each pulse frequency was set at the middle of the corresponding transition energy range. Fig. 4a and b depict these energy levels and transition energies for *p*-aminophenol with the indicated pulse frequencies. This include 5 N1s and 7 O1s excited states, respectively, as well as 10 N1sN1s and O1sO1s DCH states and 30 N1sO1s DCH states (all state energies given in Table S1†).

To set up XDQC simulations, four pulse frequencies ω_1, ω_2, ω_3, ω_4, should be specified. These were chosen to select the desired state-to-state transition energies: two from the ground–SCH state transitions (*i.e.*, XANES, or SCH state energies with ground state energy set as 0), and two from the SCH–DCH transitions, as can be seen from the pulse envelope factors in eqn (5) and (6). For instance, to generate N1sN1s intermediate DCH states, ω_1 is tuned to the N1s resonance $\omega(e^N)$, followed by the second pulse frequency ω_2 to match the energy difference between N1sN1s and N1s states, $\omega(f^{NN}) - \omega(e^N)$. ω_3 and ω_4 are then set to be $\omega(f^{NN}) - \omega(e^N)$ and $\omega(e^N)$ respectively to select the diagram-A pathway, or *vice versa* for the diagram-B pathway. Our RASSCF calculations show clear (~68 eV) separation of the two transition energies. Therefore, only one diagram (A or B) contributes given our pulse bandwidth (~10 eV), which simplifies the signal interpretation. The physical reason is as follows: two electrons in the same shell (N1s orbitals) have strong repulsion, so that $\omega(f^{NN})$ is blue shifted from twice of $\omega(e^N)$. The same applies for O1sO1s intermediate DCH states, with energies $\omega(f^{OO}) - \omega(e^O)$ and $\omega(e^O)$ differing by ~79 eV. The 2-site N1sO1s DCH states have much higher density of states (DOS) than others. A single diagram is also selected but for a different reason. Their energies (around 935 eV) can be estimated by adding the two corresponding SCH states (around 403 eV and 536 eV which sum to 939 eV; see Fig. 4a). A few eVs relaxation energy shows that the two core holes are weakly coupled, so that $\omega_{e'g}$ and $\omega_{fe'}$ difference is approximately the N1s and O1s core orbital energy difference (~130 eV).

We had examined 8 pulse configurations listed in Table 1. Based on the excitation sequences of the first two pulses (ω_1, ω_2), we classified them as ON, NO, NN, and OO to denote the SCH and DCH resonances. For example, for the ON pulse configuration, the system is excited to O1s SCH states by $\omega_1 = 536$ eV ($g \rightarrow e^O$ resonance), and then to O1sN1s DCH states by $\omega_2 = 400$ eV ($e^O \rightarrow f^{ON}$ resonance). ω_3 and ω_4 determine whether the active pathway corresponds to diagram A or B [see eqn (5) and (6)], and the full notation for pulse configuration is thus labeled as for example, ON-A. Diagram B is selected by swapping ω_3 and ω_4.

XDQC signals for *p*-aminophenol

Fig. 5 shows the simulated XDQC signals for *p*-aminophenol at 8 pulse configurations, recorded *versus* Ω_1–Ω_2. As can be seen from the denominators in eqn (5) and (6), the detection windows Ω_1, Ω_2 and Ω_3 are chosen according to the transition energy range. The Ω_1–Ω_2 plot directly correlates the SCH (ω_{eg}) and DCH (ω_{fg}) energies. Both $S_{III,A}$ and $S_{III,B}$ have the same detection windows. For instance, at ON-A and ON-B, the detection window Ω_1 is set to [532, 539] eV according to the O1s state energies, and Ω_2 set to [932, 940] eV according to the O1sN1s state energies (see respectively the denominators $\Omega_1 - \xi_{eg}$ and $\Omega_2 - \xi_{fg}$ in eqn (5) and (6)). ON and OO pulse configurations have the same Ω_1 but different Ω_2 windows ([932, 940] eV *versus* [1147, 1152] eV) as the O1sN1s and O1sO1s DCH states are respectively involved. While in the ON and NO set up, the same N1sO1s DCH states are reached *via* different paths, so they have different Ω_1 windows in accordance with the O1s and N1s state energies. We find that ON, NO, NN, OO give distinct patterns of the signals at different energy regions. While diagram A or B has a weaker influence. The signals look similar, and only differ in absolute intensities. Due to this similarity, the following discussions are limited to diagram-B, while diagram-A signals (ON-A, NO-A, NN-A, OO-A) of all isomers are given in Fig. S2–S5.† Note that diagrams A and B have different Ω_3 range ($\omega_{e'g}$ *versus* $\omega_{fe'}$), so the Ω_2–Ω_3 plot can provide complementary information. The XDQC technique can select the most sensitive channel to map and distinguish between similar structures.

XDQC signals with two-site DCH intermediates for different isomers

Fig. 6 displays the simulated XDQC signals at the ON-B pulse setting, which demonstrates the sensitivity of XDQC for resolving isomers of similar structures. Panel a recaptures the calculated O1s XANES spectra for easy comparison of the peak positions. On the Ω_1–Ω_2 plot (Fig. 6b), the strongest peak appears at $\Omega_1 = 534$ eV in all molecules. This resonates with the $g \rightarrow e_1^O$ transition (e_1^O is the first O1s core excited state), and corresponds to the strong peak 4 in the XANES spectra. *para*-Aminophenol shows a well-separated shoulder in the region 1 eV higher, in resonance with the $g \rightarrow e_2^O$ transition (peak 5 in XANES, O1s $\rightarrow \pi^*$). This shoulder is hardly seen in the other two isomers, consistent with their much weaker XANES peak 5 intensities. It is clear that the *para* isomer has more stable resonance structures or more delocalized π electrons. This feature reflects the coupling of the two groups through the π^* orbitals. The *meta* and *ortho* isomers instead exhibit more diffuse patterns in this region than the *para* one, related to the broader, unsymmetric XANES main peak 4 (O1s $\rightarrow \sigma^*_{OH}$). In addition, at $\Omega_1 = 536.7$ eV another evident feature distinguishes the 3 molecules, which strengths increased in the order of *p*-, *m*-, and *o*- isomers. The related XANES peak 6 shows almost the

same intensity. These results illustrate that XDQC can amplify the difference seen in XANES, as the more complex signal expression enforces XDQC has a stricter selectivity than XANES. A strong peak in XDQC signal requires both relatively large values of the four transition dipole moments terms and a good match in energy. Above we have identified the dominant O1s states for each peak feature. While multiple N1sO1s core excited states contribute due to their much denser DOS, and the peaks span an energy region of $\Omega_2 = 934$–936 eV.

The same Ω_2 region is found in the Ω_2–Ω_3 plot (Fig. 6c), which shows more diffuse patterns. Ω_3 is related to $e^N \rightarrow f^{ON}$ transition energies, and peaks fall in a narrow region around 533 eV. To further interpret the XDQC signals, we show the oscillator strengths between N1s SCH and O1sN1s DCH states in Fig. 7, which more vividly explains the peaks in XDQC signals. For each isomer, the strongest absorption happens at 533 eV (see bottom axes). For example, this applies to the four states $e^N_{1,2,4,5}$ in the *para* isomer. The corresponding DCH state energies are *ca.* 934 eV ($e^N_{1,2}$) and 936 eV ($e^N_{4,5}$), see top axes. The above analysis reveals the N1s states involved. The multiple contributing N1sO1s DCH states are shown by the many vertical sticks for each peak.

Fig. 8 displays signals simulated at the NO–B pulse configuration. The Ω_1–Ω_2 plot (panel a) reveals the correlation between N1s and N1sO1s states, which are sensitive to isomers. In the *para* isomer, the peaks involve double core hole states at *ca.* 934.2, 935.5, and 937.0 eV. Compared with signals at ON-B pulse setting (Fig. 6a), the active DCH states are not the same. The resonance with N1s states happens at 401.5 and 402.7 eV, which corresponds to peaks 1 and 2 respectively in N1s XANES (Fig. 3). The dominant N1s states are interpreted as e^N_1 and e^N_4, respectively, as clearly shown in Fig. 7a. The corresponding XANES peaks for the *meta* and *ortho* isomers are also peaks 1 and 2. The difference in XANES has been evidently enhanced. The *meta* isomer has broader peaks 1 and 2 (contributed from the lowest 4 states with comparable oscillator strengths), which lead to richer XDQC features than other isomers. The *ortho* isomer has a weak peak at $\Omega_1 = 404.5$ eV, which is absent in others. This is related to peak 3 in N1s XANES, where the *ortho* isomer has much larger intensity than others. The Ω_2–Ω_3 plot in Fig. 8b shows much simpler patterns. Only some of the DCH states (*ca.* 935.5 eV) contribute, as selected by the energy match and oscillator strengths between the O1s and N1sO1s states.

XDQC signals with single-site DCH intermediates for different isomers

Fig. 9 and 10 respectively show the NN-B and OO-B signals, where the 1-site DCH states are activated. The Ω_1–Ω_2 plot directly gives the correlation between SCH and DCH states, which show more isomer sensitivity than the 2-site DCH case. The N1s or O1s SCH resonances in XDQC are still limited by the corresponding XANES peak intensities. The dominant DCH sates for each feature can be more easily distinguished, as the 1-site DCHs have lower DOS. Fig. 11 gives the oscillator strengths between O1s and O1sO1s states. With this map and the O1s XANES spectra, the dominant states which contribute to the main peaks can be identified. For instance, the only major peak of *p*-aminophenol at $\Omega_1 = 534$ eV and $\Omega_2 = 1151$ eV are assigned as e^O_1 and f^{OO}_3 (Fig. 9a). They are also responsible for the main peak in the Ω_2–Ω_3 plot (Fig. 9b) at $\Omega_2 = 617$ eV. Fig. 11a shows that only state e^O_1 (bottom box) contributes at this transition energy.

Conclusions

We have implemented the state-averaged RASSCF method for simulating double core hole states in molecules and their signatures in the XDQC signals. For the three isomers of aminophenols, we have considered different intermediate DCH states on a single (N1sN1s, O1sO1s) and two sites (N1sO1s) by tuning the pulse frequencies, and interpreted the signals by comparing with the XANES spectra and the oscillator strengths between SCH and DCH states. The XDQC technique is sensitive to the correlation between SCH and DCH states and can distinguish molecules with similar structures. The Ω_1–Ω_2 plot directly records the correlation between SCH and DCH states, which shows more sensitivity to structural variations than the Ω_2–Ω_3 window. Signals recorded *via* 1-site DCH pathway are more sensitive to different isomers than the 2-site DCH one.

XDQC directly reveals the correlation of different core excited states, and thus reveals spatial correlation information inside a molecule (since core excited states are localized). In other types of nonlinear X-ray techniques, for instance, Stimulated X-ray Raman Spectroscopy (SXRS),[6] this coupling can only be inferred through valence excited states. Combining with the high temporal resolution, this spatial correlation can be used to detect ultrafast electron dynamics. This will be an interesting future direction.

RASSCF can treat various DCH and SCH states at the same theoretical level, and better incorporates the static correlation and orbital relaxation introduced by the core hole(s), which gives higher accuracy for XDQC signals than DFT-based methods used previously.[5,15] It can treat all types of 1- and 2-site DCH states accurately and can be used for simulations of other nonlinear X-ray signals involving DCHs. More accurate energies can be expected from a multi-state RASPT2 method. RASSCF also gives a reasonable estimate of the absolute core excitation energies. Creating a DCH on the same shell requires higher energy than twice of the energy to create a SCH. Creating a DCH on two weakly coupled orbitals (*e.g.*, N1s and O1s in aminophenols) requires approximately the sum of energies used to create an individual SCH. Both cases show good energy separation and the signals are dominated by a single diagram, which simplifies the interpretation of the signals. The 2-site DCH of the same element and shell (*e.g.*, a 2-site DCH on the C_α 1s and C_β 1s orbitals in furan which separate by 1 eV (ref. 67)) is an interesting issue for future study.

XDQC signals with two-site double core hole intermediates can reveal the coupling of the two core holes. In our aminophenol models, both side groups are electron donors. When one group is changed to an acceptor, it can represent a large class of push–pull chromophores (also known as donor–acceptor molecules; *e.g.*, *p*-nitrophenolate, *p*-aminobenzoic

acid) which show intramolecular charge transfer transitions and serve as building blocks of optical materials.[68] By properly tuning two-site DCH excitations on the two side groups, the XDQC signals could provide a novel probe for intramolecular charge transfer.

Computational methods

Electronic structure

Geometries were optimized at the B3LYP/aug-cc-pVTZ[69] level with the Gaussian 09 program.[70] All valence, SCH, and DCH states were calculated with the cc-pVDZ basis set[71] by using the Molpro2012 program.[72] SA-CASSCF method with 6 orbitals and 6 electrons were used to generate the 10 low-lying valence states, though only the lowest root (ground state) was used in signal calculations. SCH and DCH states were computed starting from the converged valence wavefunction. The excited core orbital was chosen in the RAS1 space with freezed occupation, which the size being 1 for the SCH and 1-site DCH states, and 2 for the 2-site DCH states. 2 orbitals were set in the RAS2 space, and 15 orbitals in the RAS3 space. 30 states were calculated spanning an energy range of several eVs. With resulting wavefunctions, TDMs between the ground and SCH states ($\mathbf{V}_{\mathrm{ge}}$) and between the SCH and DCH states ($\mathbf{V}_{\mathrm{ef}}$) as well as the XDQC signals were then calculated by our in-house code. For instance, $\mathbf{V}_{\mathrm{ef}}$ is given by

$$\boldsymbol{V}_{\mathrm{ef}} = \langle \Phi_{\mathrm{e}}|\hat{\mu}|\Psi_{\mathrm{f}}\rangle = \sum_i \sum_j \left(\lambda_j^{\mathrm{e}}\right)^* \kappa_i^{\mathrm{f}} \left\langle \phi_j^{\mathrm{e}}|\hat{\mu}|\psi_i^{\mathrm{f}}\right\rangle, \quad (1)$$

where $|\Phi_{\mathrm{e}}\rangle = \sum_j \lambda_j^{\mathrm{e}} \left|\phi_j^{\mathrm{e}}\right\rangle$ and $\left|\Psi_{\mathrm{f}}\right\rangle = \sum_i \kappa_i^{\mathrm{f}} \left|\psi_i^{\mathrm{f}}\right\rangle$ are the SA-RASSCF wavefunctions for the SCH and DCH states, with $|\phi_j^{\mathrm{e}}\rangle$ and $|\psi_i^{\mathrm{f}}\rangle$ the Slater's determinants, and λ_j^{e} and κ_i^{e} the CI coefficients. $\langle\phi_j^{\mathrm{e}}|\hat{\mu}|\psi_i^{\mathrm{f}}\rangle$ were calculated using the Löwdin rules.[73]

XANES spectra

The N1s and O1s XANES spectra were first calculated for all molecules. The orientationally averaged oscillator strengths are given by

$$F_{\mathrm{eg}} = \frac{2m\omega_{\mathrm{eg}}}{3\hbar}\left|\mathbf{V}_{\mathrm{eg}}\right|^2. \quad (2)$$

To calibrate our simulations, we had calculated the spectra of *p*-aminophenol at different levels of theory, including RASSCF with two different active spaces (6, 1/4/14) and (4, 1/2/15), and the static and the time-dependent DFT methods with the B3LYP functional. DFT-FCH calculations were performed by the GAMESS-US package[74] (maximum overlap method[75] used for SCF convergence) and DFT-ECH calculations by the Gaussian 09 package. The IGLO-III basis set[76] was set for the excited atom while the cc-pVDZ basis for the rest. With wavefunctions and integrals in hand, spectra were generated with our in-house code. The restricted excitation window TDDFT/TDA calculations were performed using the NWChem package[50,77] with the cc-pVDZ basis for all atoms.

Calibration was first carried out for the DFT-FCH method using the ΔKS scheme.[61] The IP was calculated as the energy difference between FCH and ground state. N1s (O1s) core excited state energies were then uniformly shifted by 0.21 (0.38) eV to include the scalar relativistic effect for the core hole.[62] Such a protocol can yield transition energies in good agreement with experiment. Stick spectra were convoluted with a Gaussian line shape with hwhm of 0.3 eV. Then, resolved spectra from other methods were calibrated by aligning the first resolved main peak (shifts given in caption of Fig. 2). *Meta* and *ortho*-aminophenols were only calculated at the DFT-FCH and RASSCF (4, 1/2/15) levels, and the same set of shift values as *p*-aminophenol was obtained. The DCH state energies were taken as sums of the shifts of the corresponding SCH states.[15]

XDQC signals

The XDQC signals were calculated using Gaussian pulse shapes with duration of $\sigma_j = 100$ as ($j = 1, 2, 3, 4$), which spans an energy bandwidth of 10.96 eV (fwhm in power spectrum). 8 pulse carrier frequencies were set to select different double core excitations (N1sN1s, O1sO1s, N1sO1s) and different pathways (diagrams A and B). We performed Fourier transformation of the 3D frequency-domain signal, with respect to either Ω_3 or Ω_1 to obtain $S_{\mathrm{III}}(\Omega_3, \Omega_2, t_1 = 0\ \mathrm{fs})$ and $S_{\mathrm{III}}(t_3 = 6.1\ \mathrm{fs}, \Omega_2, \Omega_1)$, see eqn (7) and (8). The core hole lifetime broadening have been chosen as follows: 0.01 eV for ground state, 0.09 eV and 0.13 eV for N1s and O1s SCH states,[78] and 0.4 eV for all DCH states. The lifetime broadening for DCH excited states was set larger than the SCH states. We had tested different DCH lifetime parameters, these only lead to elongation/compression of the 2D signals along the Ω_2 axis and does not affect our analysis.

Appendix

Sum-over-states expressions for XDQC signals

The X-ray electric field at time t and position $\mathbf{r}$ is given by

$$\boldsymbol{E}(t) = \sum_{j=1}^{4} \mathbf{e}_j \mathscr{E}_j(t-\tau_j)\exp\left[\mathrm{i}\mathbf{k}_j\cdot\mathbf{r} - \mathrm{i}\omega_j(t-\tau_j)\right] + \mathrm{c.c.} \quad (3)$$

Here $\mathscr{E}_j(t-\tau_j)$ denotes the complex envelope of the jth pulse, and $\mathbf{e}_j$ is the electric polarization vector. We assumed a Gaussian envelope $\mathscr{E}_j(t-\tau_j) = A_j \exp\left[-\frac{(t-\tau_j)^2}{2\sigma_j^2}\right]$ for all pulses with σ_j the pulse duration, and A_j the complex amplitude. The pulse spectral envelope is given by

$$\begin{aligned}\mathscr{E}_j(\omega) &= \int_{-\infty}^{+\infty} \mathrm{d}t \mathscr{E}_j(t-\tau_j)\mathrm{e}^{\mathrm{i}\omega t} \\ &= A_j\sqrt{2\pi}\sigma_j \exp(\mathrm{i}\omega\tau_j)\exp\left(-\frac{\sigma_j^2\omega^2}{2}\right).\end{aligned}$$

The sum-over-states $\mathbf{k}_{\mathrm{III}}$ signal is given by[14,15]

$$S_{\mathrm{III}}(\Omega_3,\Omega_2,\Omega_1) = S_{\mathrm{III,A}}(\Omega_3,\Omega_2,\Omega_1) + S_{\mathrm{III,B}}(\Omega_3,\Omega_2,\Omega_1), \quad (4)$$

with

$$S_{\mathrm{III,A}}(\Omega_3,\Omega_2,\Omega_1)=\sum_{\mathrm{fe'e}}\mathscr{E}_4^*(\omega_4-\omega_{\mathrm{e'g}})\mathscr{E}_3^*(\omega_3-\omega_{\mathrm{fe'}})\mathscr{E}_2(\omega_2-\omega_{\mathrm{fe}})\times\mathscr{E}_1(\omega_1-\omega_{\mathrm{eg}})\frac{\mathbf{V}_{\mathrm{ge'}}\cdot\mathbf{e}_4}{(\Omega_3-\xi_{\mathrm{e'g}})}\frac{(\mathbf{V}_{\mathrm{e'f}}\cdot\mathbf{e}_3)(\mathbf{V}_{\mathrm{fe}}\cdot\mathbf{e}_2)}{(\Omega_2-\xi_{\mathrm{fg}})}\frac{\mathbf{V}_{\mathrm{eg}}\cdot\mathbf{e}_1}{(\Omega_1-\xi_{\mathrm{eg}})},\tag{5}$$

$$S_{\mathrm{III,B}}(\Omega_3,\Omega_2,\Omega_1)=-\sum_{\mathrm{fe'e}}\mathscr{E}_4^*(\omega_4-\omega_{\mathrm{fe'}})\mathscr{E}_3^*(\omega_3-\omega_{\mathrm{e'g}})\mathscr{E}_2(\omega_2-\omega_{\mathrm{fe}})\times\mathscr{E}_1(\omega_1-\omega_{\mathrm{eg}})\frac{\mathbf{V}_{\mathrm{e'f}}\cdot\mathbf{e}_4}{(\Omega_3-\xi_{\mathrm{fe'}})}\frac{(\mathbf{V}_{\mathrm{ge'}}\cdot\mathbf{e}_3)(\mathbf{V}_{\mathrm{fe}}\cdot\mathbf{e}_2)}{(\Omega_2-\xi_{\mathrm{fg}})}\frac{\mathbf{V}_{\mathrm{eg}}\cdot\mathbf{e}_1}{(\Omega_1-\xi_{\mathrm{eg}})},\tag{6}$$

referring to two contributing terms that can be respectively read off the two diagrams in Fig. 1c. g denotes the ground state, e and e′ stand for SCH states, and f are DCH states. $\xi_{\alpha\beta}=\omega_{\alpha\beta}-\mathrm{i}\gamma_{\alpha\beta}$, where $\omega_{\alpha\beta}=\varepsilon_\alpha-\varepsilon_\beta$ stands for the transition energy between states α and β, and $\gamma_{\alpha\beta}=\gamma_\alpha+\gamma_\beta$ with $\gamma_{\alpha(\beta)}$ the lifetime broadening of state α(β). Fourier transformation over Ω_3 or Ω_1 lead respectively to

$$S_{\mathrm{III}}(t_3,\Omega_2,\Omega_1)=\int_{-\infty}^{\infty}\mathrm{e}^{-\mathrm{i}\Omega_3 t_3}S_{\mathrm{III}}(\Omega_3,\Omega_2,\Omega_1),\tag{7}$$

$$S_{\mathrm{III}}(\Omega_3,\Omega_2,t_1)=\int_{-\infty}^{\infty}\mathrm{e}^{-\mathrm{i}\Omega_1 t_1}S_{\mathrm{III}}(\Omega_3,\Omega_2,\Omega_1).\tag{8}$$

We took all parallel pulse configurations and considered the orientationally averaged given by[15]

$$S_{\mathrm{III}}^{\mathrm{aver}}=\frac{1}{15}\sum_{\xi,\eta=x,y,z}\left(S_{\mathrm{III}}^{\eta\eta\xi\xi}+S_{\mathrm{III}}^{\eta\xi\eta\xi}+S_{\mathrm{III}}^{\xi\eta\eta\xi}\right).\tag{9}$$

Acknowledgements

The support of the Chemical Sciences, Geosciences and Biosciences Division, Office of Basic Energy Sciences, Office of Science, U.S. Department of Energy (DOE) through award no. DE-FG02-4ER15571 and the National Science Foundation award CHE-1361516 is gratefully acknowledged. WH was supported by the DOE grant at UCI. S. M. wishes to thank the Freiburg Institite of Advanced Science (FRIAS) for their support. The work at KTH was supported by Knut and Alice Wallenberg Foundation (Grant No. KAW-2013.0020) for the project "Strong Field Physics and New States of Matter", Göran Gustafsson Foundation for Research in Natural Sciences and Medicine, and the Hefei Science Center CAS (2015HSC-UE008). This research used resources of the National Energy Research Scientific Computing Center, a DOE Office of Science User Facility supported by the Office of Science of the U.S. Department of Energy under Contract No. DE-AC02-05CH11231 and from the Swedish National Infrastructure for Computing (SNIC).

References

1 J. Stöhr, *NEXAFS Spectroscopy*, Springer, Berlin, 1992.
2 (*a*) P. Emma, R. Akre, J. Arthur, R. Bionta, C. Bostedt, J. Bozek, A. Brachmann, P. Bucksbaum, R. Coffee, F.-J. Decker, Y. Ding, D. Dowell, S. Edstrom, A. Fisher, J. Frisch, S. Gilevich, J. Hastings, G. Hays, P. Hering, Z. Huang, R. Iverson, H. Loos, M. Messerschmidt, A. Miahnahri, S. Moeller, H.-D. Nuhn, G. Pile, D. Ratner, J. Rzepiela, D. Schultz, T. Smith, P. Stefan, H. Tompkins, J. Turner, J. Welch, W. White, J. Wu, G. Yocky and J. Galayda, *Nat. Photonics*, 2010, **4**, 641–647; (*b*) J. Ullrich, A. Rudenko and R. Moshammer, *Annu. Rev. Phys. Chem.*, 2012, **63**, 635–660.
3 (*a*) J. Krause, K. Schafer and K. Kulander, *Phys. Rev. Lett.*, 1992, **68**, 3535–3538; (*b*) P. Corkum, *Phys. Rev. Lett.*, 1993, **71**, 1994–1997; (*c*) H. Kapteyn, O. Cohen, I. Christov and M. Murnane, *Science*, 2007, **317**, 775–778; (*d*) K. T. Kim, D. M. Villeneuve and P. B. Corkum, *Nat. Photonics*, 2014, **8**, 187–194.
4 I. V. Schweigert and S. Mukamel, *Phys. Rev. Lett.*, 2007, **99**, 163001.
5 V. Schweigert and S. Mukamel, *Phys. Rev. A: At., Mol., Opt. Phys.*, 2008, **78**, 052509.
6 J. D. Biggs, Y. Zhang, D. Healion and S. Mukamel, *J. Chem. Phys.*, 2012, **136**, 174117.
7 S. Mukamel, D. Healion, Y. Zhang and J. D. Biggs, *Annu. Rev. Phys. Chem.*, 2013, **64**, 101–127.
8 Y. Zhang, W. Hua, K. Bennett and S. Mukamel, *Top. Curr. Chem.*, 2016, **368**, 273–345.
9 T. E. Glover, D. M. Fritz, M. Cammarata, T. K. Allison, S. Coh, J. M. Feldkamp, H. Lemke, D. Zhu, Y. Feng, R. N. Coffee, M. Fuchs, S. Ghimire, J. Chen, S. Shwartz, D. A. Reis, S. E. Harris and J. B. Hastings, *Nature*, 2012, **488**, 603–608.
10 M. Beye, S. Schreck, F. Sorgenfrei, C. Trabant, N. Pontius, C. Schüßler-Langeheine, W. Wurth and A. Föhlisch, *Nature*, 2013, **501**, 191–194.
11 P. Wernet, K. Kunnus, I. Josefsson, I. Rajkovic, W. Quevedo, M. Beye, S. Schreck, S. Grübel, M. Scholz, D. Nordlund, W. Zhang, R. W. Hartsock, W. F. Schlotter, J. J. Turner, B. Kennedy, F. Hennies, F. M. F. de Groot, K. J. Gaffney, S. Techert, M. Odelius and A. Föhlisch, *Nature*, 2015, **520**, 78–81.
12 F. Bencivenga, M. Zangrando, C. Svetina, A. Abrami, A. Battistoni, R. Borghes, F. Capotondi, R. Cucini, F. Dallari, M. Danailov, A. Demidovich, C. Fava, G. Gaio, S. Gerusina, A. Gessini, F. Giacuzzo, R. Gobessi, R. Godnig, R. Grisonich, M. Kiskinova, G. Kurdi, G. Loda, M. Lonza, N. Mahne, M. Manfredda, R. Mincigrucci, G. Pangon, P. Parisse, R. Passuello, E. Pedersoli, L. Pivetta, M. Prica, E. Principi, I. Rago, L. Raimondi, R. Sauro, M. Scarcia, P. Sigalotti, M. Zaccaria and C. Masciovecchio, *J. Synchrotron Radiat.*, 2016, **23**, 132–140.
13 F. Bencivenga, R. Cucini, F. Capotondi, A. Battistoni, R. Mincigrucci, E. Giangrisostomi, A. Gessini, M. Manfredda, I. P. Nikolov, E. Pedersoli, E. Principi, C. Svetina, P. Parisse, F. Casolari, M. B. Danailov, M. Kiskinova and C. Masciovecchio, *Nature*, 2015, **520**, 205–208.
14 D. Abramavicius, B. Palmieri, D. V. Voronine, F. Šanda and S. Mukamel, *Chem. Rev.*, 2009, **109**, 2350–2408.

15 Y. Zhang, D. Healion, J. D. Biggs and S. Mukamel, *J. Chem. Phys.*, 2013, **138**, 144301.
16 S. Mukamel, D. Abramavicius, L. Yang, W. Zhuang, I. V. Schweigert and D. V. Voronine, *Acc. Chem. Res.*, 2009, **42**, 553–562.
17 J. D. Biggs, J. A. Voll and S. Mukamel, *Philos. Trans. R. Soc. London, Ser. A*, 2012, **370**, 3709–3727.
18 L. S. Cederbaum, F. Tarantelli, A. Sgamellotti and J. Schirmer, *J. Chem. Phys.*, 1986, **85**, 6513–6523.
19 L. S. Cederbaum, *Phys. Rev. A: At., Mol., Opt. Phys.*, 1987, **35**, 622–631.
20 A. A. Sorokin, S. V. Bobashev, T. Feigl, K. Tiedtke, H. Wabnitz and M. Richter, *Phys. Rev. Lett.*, 2007, **99**, 213002.
21 L. Young, E. P. Kanter, B. Krässig, Y. Li, A. M. March, S. T. Pratt, R. Santra, S. H. Southworth, N. Rohringer, L. F. DiMauro, G. Doumy, C. A. Roedig, N. Berrah, L. Fang, M. Hoener, P. H. Bucksbaum, J. P. Cryan, S. Ghimire, J. M. Glownia, D. A. Reis, J. D. Bozek, C. Bostedt and M. Messerschmidt, *Nature*, 2010, **466**, 56–61.
22 L. J. Frasinski, V. Zhaunerchyk, M. Mucke, R. J. Squibb, M. Siano, J. H. D. Eland, P. Linusson, P. v. d. Meulen, P. Salén, R. D. Thomas, M. Larsson, L. Foucar, J. Ullrich, K. Motomura, S. Mondal, K. Ueda, T. Osipov, L. Fang, B. F. Murphy, N. Berrah, C. Bostedt, J. D. Bozek, S. Schorb, M. Messerschmidt, J. M. Glownia, J. P. Cryan, R. N. Coffee, O. Takahashi, S. Wada, M. N. Piancastelli, R. Richter, K. C. Prince and R. Feifel, *Phys. Rev. Lett.*, 2013, **111**, 073002.
23 J. H. D. Eland, M. Tashiro, P. Linusson, M. Ehara, K. Ueda and R. Feifel, *Phys. Rev. Lett.*, 2010, **105**, 213005.
24 P. Lablanquie, T. P. Grozdanov, M. Žitnik, S. Carniato, P. Selles, L. Andric, J. Palaudoux, F. Penent, H. Iwayama, E. Shigemasa, Y. Hikosaka, K. Soejima, M. Nakano, I. H. Suzuki and K. Ito, *Phys. Rev. Lett.*, 2011, **107**, 193004.
25 P. Lablanquie, F. Penent, J. Palaudoux, L. Andric, P. Selles, S. Carniato, K. Bučar, M. Žitnik, M. Huttula, J. H. D. Eland, E. Shigemasa, K. Soejima, Y. Hikosaka, I. H. Suzuki, M. Nakano and K. Ito, *Phys. Rev. Lett.*, 2011, **106**, 063003.
26 N. V. Kryzhevoi, R. Santra and L. S. Cederbaum, *J. Chem. Phys.*, 2011, **135**, 084302.
27 N. Berrah, L. Fang, B. Murphy, T. Osipov, K. Ueda, E. Kukk, R. Feifel, P. v. d. Meulen, P. Salen, H. T. Schmidt, R. D. Thomas, M. Larsson, R. Richter, K. C. Prince, J. D. Bozek, C. Bostedt, S.-i. Wada, M. N. Piancastelli, M. Tashiro and M. Ehara, *Proc. Natl. Acad. Sci. U. S. A.*, 2011, **108**, 16912–16915.
28 P. Linusson, O. Takahashi, K. Ueda, J. H. D. Eland and R. Feifel, *Phys. Rev. A: At., Mol., Opt. Phys.*, 2011, **83**, 022506.
29 P. Salén, P. van der Meulen, H. T. Schmidt, R. D. Thomas, M. Larsson, R. Feifel, M. N. Piancastelli, L. Fang, B. Murphy, T. Osipov, N. Berrah, E. Kukk, K. Ueda, J. D. Bozek, C. Bostedt, S. Wada, R. Richter, V. Feyer and K. C. Prince, *Phys. Rev. Lett.*, 2012, **108**, 153003.
30 M. Mucke, J. H. D. Eland, O. Takahashi, P. Linusson, D. Lebrun, K. Ueda and R. Feifel, *Chem. Phys. Lett.*, 2013, **558**, 82–87.
31 M. Nakano, P. Selles, P. Lablanquie, Y. Hikosaka, F. Penent, E. Shigemasa, K. Ito and S. Carniato, *Phys. Rev. Lett.*, 2013, **111**, 123001.
32 M. Nakano, F. Penent, M. Tashiro, T. P. Grozdanov, M. Žitnik, S. Carniato, P. Selles, L. Andric, P. Lablanquie, J. Palaudoux, E. Shigemasa, H. Iwayama, Y. Hikosaka, K. Soejima, I. H. Suzuki, N. Kouchi and K. Ito, *Phys. Rev. Lett.*, 2013, **110**, 163001.
33 (*a*) S. Carniato, P. Selles, L. Andric, J. Palaudoux, F. Penent, M. Žitnik, K. Bučar, M. Nakano, Y. Hikosaka, K. Ito and P. Lablanquie, *J. Chem. Phys.*, 2015, **142**, 014307; (*b*) S. Carniato, P. Selles, L. Andric, J. Palaudoux, F. Penent, M. Žitnik, K. Bučar, M. Nakano, Y. Hikosaka, K. Ito and P. Lablanquie, *J. Chem. Phys.*, 2015, **142**, 014308.
34 V. Zhaunerchyk, M. Kamińska, M. Mucke, R. J. Squibb, J. H. D. Eland, M. N. Piancastelli, L. J. Frasinski, J. Grilj, M. Koch, B. K. McFarland, E. Sistrunk, M. Gühr, R. N. Coffee, C. Bostedt, J. D. Bozek, P. Salén, P. v. d. Meulen, P. Linusson, R. D. Thomas, M. Larsson, L. Foucar, J. Ullrich, K. Motomura, S. Mondal, K. Ueda, R. Richter, K. C. Prince, O. Takahashi, T. Osipov, L. Fang, B. F. Murphy, N. Berrah and R. Feifel, *J. Phys. B: At., Mol. Opt. Phys.*, 2015, **48**, 244003.
35 M. Mucke, V. Zhaunerchyk, L. J. Frasinski, R. J. Squibb, M. Siano, J. H. D. Eland, P. Linusson, P. Salén, P. v. d. Meulen, R. D. Thomas, M. Larsson, L. Foucar, J. Ullrich, K. Motomura, S. Mondal, K. Ueda, T. Osipov, L. Fang, B. F. Murphy, N. Berrah, C. Bostedt, J. D. Bozek, S. Schorb, M. Messerschmidt, J. M. Glownia, J. P. Cryan, R. N. Coffee, O. Takahashi, S. Wada, M. N. Piancastelli, R. Richter, K. C. Prince and R. Feifel, *New J. Phys.*, 2015, **17**, 073002.
36 J. H. D. Eland, S. Plogmaker, P. Lablanquie, F. Penent, J. Palaudoux, C. Nicolas, E. Robert, C. Miron and R. Feifel, *Chem. Phys. Lett.*, 2016, **646**, 31–35.
37 F. Penent, M. Nakano, M. Tashiro, T. P. Grozdanov, M. Žitnik, K. Bučar, S. Carniato, P. Selles, L. Andric, P. Lablanquie, J. Palaudoux, E. Shigemasa, H. Iwayama, Y. Hikosaka, K. Soejima, I. H. Suzuki, N. Berrah, A. H. Wuosmaa, T. Kaneyasu and K. Ito, *J. Electron Spectrosc. Relat. Phenom.*, 2015, **204**, 303–312.
38 O. Takahashi, N. V. Kryzhevoi and K. Ueda, *J. Electron Spectrosc. Relat. Phenom.*, 2015, **204**, 290–302.
39 J. P. Cryan, J. M. Glownia, J. Andreasson, A. Belkacem, N. Berrah, C. I. Blaga, C. Bostedt, J. Bozek, C. Buth, L. F. DiMauro, L. Fang, O. Gessner, M. Guehr, J. Hajdu, M. P. Hertlein, M. Hoener, O. Kornilov, J. P. Marangos, A. M. March, B. K. McFarland, H. Merdji, V. S. Petrović, C. Raman, D. Ray, D. Reis, F. Tarantelli, M. Trigo, J. L. White, W. White, L. Young, P. H. Bucksbaum and R. N. Coffee, *Phys. Rev. Lett.*, 2010, **105**, 083004.
40 S. Bodeur, P. Millié, E. Lizon, I. Nenner, A. Filipponi, F. Boscherini and S. Mobilio, *Phys. Rev. A: At., Mol., Opt. Phys.*, 1989, **39**, 5075–5081.
41 H. Ågren and H. J. Å. Jensen, *Chem. Phys.*, 1993, **172**, 45–57.

42 (*a*) M. Tashiro, M. Ehara, H. Fukuzawa, K. Ueda, C. Buth, N. V. Kryzhevoi and L. S. Cederbaum, *J. Chem. Phys.*, 2010, **132**, 184302; (*b*) M. Tashiro, M. Ehara and K. Ueda, *Chem. Phys. Lett.*, 2010, **496**, 217–222; (*c*) O. Takahashi, M. Tashiro, M. Ehara, K. Yamasaki and K. Ueda, *Chem. Phys.*, 2011, **384**, 28–35; (*d*) M. Tashiro, K. Ueda and M. Ehara, *Chem. Phys. Lett.*, 2012, **521**, 45–51.

43 (*a*) P. Kolorenč, V. Averbukh, K. Gokhberg and L. S. Cederbaum, *J. Chem. Phys.*, 2008, **129**, 244102; (*b*) R. Santra, N. V. Kryzhevoi and L. S. Cederbaum, *Phys. Rev. Lett.*, 2009, **103**, 013002; (*c*) V. Stumpf, K. Gokhberg and L. S. Cederbaum, *Nat. Chem.*, 2016, **8**, 237–241.

44 T. D. Thomas, *J. Phys. Chem. A*, 2012, **116**, 3856–3865.

45 S. Mukamel, *Principles of nonlinear optical spectroscopy*, Oxford University Press, New York, Oxford, 1999.

46 (*a*) W. L. Jolly and D. N. Hendrickson, *J. Am. Chem. Soc.*, 1970, **92**, 1863; (*b*) D. W. Davis and D. A. Shirley, *Chem. Phys. Lett.*, 1972, **15**, 185; (*c*) O. Plashkevych, T. Privalov, H. Ågren, V. Carravetta and K. Ruud, *Chem. Phys.*, 2000, **260**, 11.

47 W. Hua, B. Gao and Y. Luo, *Prog. Chem.*, 2012, **24**, 964–980.

48 (*a*) B. Brena, Y. Luo, M. Nyberg, S. Carniato, K. Nilson, Y. Alfredsson, J. Åhlund, N. Mårtensson, H. Siegbahn and C. Puglia, *Phys. Rev. B*, 2004, **70**, 195214; (*b*) B. Brena, S. Carniato and Y. Luo, *J. Chem. Phys.*, 2005, **122**, 184316.

49 D. Prendergast and G. Galli, *Phys. Rev. Lett.*, 2006, **96**, 215502.

50 K. Lopata, B. E. V. Kuilen, M. Khalil and N. Govind, *J. Chem. Theory Comput.*, 2012, **8**, 3284.

51 (*a*) M. Casida, A. Ipatov and F. Cordova, *Time-Dependent Density Functional Theory*, Spinger-Verlag, Berlin, 2006, vol. 706, p. 243; (*b*) A. Ipatov, F. Cordova, L. J. Doriol and M. E. Casida, *J. Mol. Struct.: THEOCHEM*, 2009, **914**, 60–73.

52 P. A. Malmqvist, B. O. Roos and B. Schimmelpfennig, *Chem. Phys. Lett.*, 2002, **357**, 230–240.

53 (*a*) H. J. A. Jensen, P. Jørgensen and H. Ågren, *J. Chem. Phys.*, 1987, **87**, 451–466; (*b*) H. Ågren and H. J. Å. Jensen, *Chem. Phys. Lett.*, 1987, **137**, 431–436; (*c*) H. Ågren, A. Flores-Riveros and H. J. Å. Jensen, *Phys. Scr.*, 1989, **40**, 745.

54 I. Josefsson, K. Kunnus, S. Schreck, A. Föhlisch, F. de Groot, P. Wernet and M. Odelius, *J. Phys. Chem. Lett.*, 2012, **3**, 3565–3570.

55 (*a*) P. Wernet, K. Kunnus, S. Schreck, W. Quevedo, R. Kurian, S. Techert, F. M. F. de Groot, M. Odelius and A. Föhlisch, *J. Phys. Chem. Lett.*, 2012, **3**, 3448–3453; (*b*) K. Atak, S. I. Bokarev, M. Gotz, R. Golnak, K. M. Lange, N. Engel, M. Dantz, E. Suljoti, O. Kühn and E. F. Aziz, *J. Phys. Chem. B*, 2013, **117**, 12613–12618; (*c*) S. I. Bokarev, M. Dantz, E. Suljoti, O. kühn and E. F. Aziz, *Phys. Rev. Lett.*, 2013, **111**, 083002; (*d*) E. Suljoti, R. Garcia-Diez, S. I. Bokarev, K. M. Lange, R. Schoch, B. Dierker, M. Dantz, K. Yamamoto, N. Engel, K. Atak, O. Kühn, M. Bauer, J.-E. Rubensson and E. F. Aziz, *Angew. Chem., Int. Ed.*, 2013, **52**, 9841–9844; (*e*) R. V. Pinjari, M. G. Delcey, M. Guo, M. Odelius and M. Lundberg, *J. Chem. Phys.*, 2014, **141**, 124116; (*f*) K. Kunnus, I. Josefsson, I. Rajkovic, S. Schreck, W. Quevedo, M. Beye, C. Weniger, S. Grübel, M. Scholz, D. Nordlund, W. Zhang, R. W. Hartsock, K. J. Gaffney, W. F. Schlotter, J. J. Turner, B. Kennedy, F. Hennies, F. M. F. de Groot, S. Techert, M. Odelius, P. Wernet and A. Föhlisch, *Struct. Dyn.*, 2016, **3**, 043204; (*g*) M. Guo, L. K. Sørensen, M. G. Delcey, R. V. Pinjari and M. Lundberg, *Phys. Chem. Chem. Phys.*, 2016, **18**, 3250–3259.

56 R. V. Pinjari, M. G. Delcey, M. Guo, M. Odelius and M. Lundberg, *J. Comput. Chem.*, 2016, **37**, 477–486.

57 W. Hua, S. Oesterling, J. D. Biggs, Y. Zhang, H. Ando, R. de Vivie-Riedle, B. P. Fingerhut and S. Mukamel, *Struct. Dyn.*, 2016, **3**, 023601.

58 J. Finley, P. Malmqvist, B. O. Roos and L. Serrano-Andrés, *Chem. Phys. Lett.*, 1998, **288**, 299–306.

59 S. C. Mitchell, P. Carmichael and R. Waring, *Kirk-Othmer Encyclopedia of Chemical Technology*, John Wiley & Sons, Inc., 2000.

60 N. Chouhan, M. L. Kalra, S. Kumar, Y. N. Singh and S. C. Ameta, *Mol. Cryst. Liq. Cryst.*, 2007, **469**, 99–110.

61 (*a*) P. S. Bagus, *Phys. Rev.*, 1965, **139**, A619–A634; (*b*) L. Triguero, O. Plashkevych, L. G. M. Pettersson and H. Ågren, *J. Electron Spectrosc. Relat. Phenom.*, 1999, **104**, 195–207.

62 L. Triguero, L. G. M. Pettersson and H. Ågren, *Phys. Rev. B: Condens. Matter*, 1998, **58**, 8097–8110.

63 S. Hirata and M. Head-Gordon, *Chem. Phys. Lett.*, 1999, **314**, 291–299.

64 (*a*) A. D. Becke, *Phys. Rev. A: At., Mol., Opt. Phys.*, 1988, **38**, 3098–3100; (*b*) A. D. Becke, *J. Chem. Phys.*, 1993, **98**, 5648; (*c*) C. Lee, W. Yang and R. G. Parr, *Phys. Rev. B*, 1988, **37**, 785–789.

65 (*a*) G. Fronzoni, O. Baseggio, M. Stener, W. Hua, G. Tian, Y. Luo, B. Apicella, M. Alfé, M. d. Simone, A. Kivimäki and M. Coreno, *J. Chem. Phys.*, 2014, **141**, 044313; (*b*) W. Hua, H. Yamane, B. Gao, J. Jiang, S. Li, H. S. Kato, M. Kawai, T. Hatsui, Y. Luo, N. Kosugi and H. Ågren, *J. Phys. Chem. B*, 2010, **114**, 7016–7021.

66 H. Li, W. Hua, Z. Lin and Y. Luo, *J. Phys. Chem. B*, 2012, **116**, 12641–12650.

67 W. Hua, J. D. Biggs, Y. Zhang, D. Healion, H. Ren and S. Mukamel, *J. Chem. Theory Comput.*, 2013, **9**, 5479–5489.

68 (*a*) M. J. Cho, D. H. Choi, P. A. Sullivan, A. J. P. Akelaitis and L. R. Dalton, *Prog. Polym. Sci.*, 2008, **33**, 1013–1058; (*b*) M.-B. Suhr Kirketerp, M. Åxman Petersen, M. Wanko, L. Andres Espinosa Leal, H. Zettergren, F. M. Raymo, A. Rubio, M. Brøndsted Nielsen and S. Brøndsted Nielsen, *ChemPhysChem*, 2009, **10**, 1207–1209; (*c*) M. Wanko, J. Houmøller, K. Støchkel, M.-B. S. Kirketerp, M. Å. Petersen, M. B. Nielsen, S. B. Nielsen and A. Rubio, *Phys. Chem. Chem. Phys.*, 2012, **14**, 12905–12911; (*d*) A. G. Thomas, M. J. Jackman, M. Wagstaffe, H. Radtke, K. Syres, J. Adell, A. Lévy and N. Martsinovich, *Langmuir*, 2014, **30**, 12306–12314.

69 R. A. Kendall, T. H. Dunning Jr and R. J. Harrison, *J. Chem. Phys.*, 1992, **96**, 6796–6806.

70 M. J. Frisch, G. W. Trucks, H. B. Schlegel, G. E. Scuseria and M. A. Robb *et al.*, *Gaussian 09 Revision D.01*, Gaussian Inc., Wallingford CT, 2009.

71 T. H. Dunning, *J. Chem. Phys.*, 1989, **90**, 1007–1023.

72 H.-J. Werner, P. J. Knowles, G. Knizia, F. R. Manby and M. Schütz *et al.*, *MOLPRO, version 2012.1, a package of ab initio programs*, 2012, see http://www.molpro.net.

73 (*a*) P.-O. Löwdin, *Phys. Rev.*, 1955, **97**, 1474–1489; (*b*) D. B. Cook, *Handbook of computational quantum chemistry*, Dover Publications, Mineola, N.Y., 2005, pp. 66–69.

74 (*a*) M. W. Schmidt, K. K. Baldridge, J. A. Boatz, S. T. Elbert, M. S. Gordon, J. H. Jensen, S. Koseki, N. Matsunaga, K. A. Nguyen, S. Su, T. L. Windus, M. Dupuis and J. A. Montgomery Jr, *J. Comput. Chem.*, 1993, **14**, 1347–1363; (*b*) M. S. Gordon and M. W. Schmidt, in *Advances in electronic structure theory: GAMESS a decade later*, ed. C. E. Dykstra, G. Frenking, K. S. Kim and G. E. Scuseria, Elsevier, Amsterdam, 2005, ch. 41, pp. 1167–1189; (*c*) http://www.msg.chem.iastate.edu/GAMESS/GAMESS.html.

75 A. T. B. Gilbert, N. A. Besley and P. M. W. Gill, *J. Phys. Chem. A*, 2008, **112**, 13164–13171.

76 W. Kutzelnigg and U. Fleischer and M. Schindler, in *NMR Basic Principles and Progress*, Springer Verlag, Heidelberg, 1990, vol. 23, p. 165.

77 M. Valiev, E. Bylaska, N. Govind, K. Kowalski, T. Straatsma, H. Van Dam, D. Wang, J. Nieplocha, E. Apra, T. Windus and W. de Jong, *Comput. Phys. Commun.*, 2010, **181**, 1477–1489.

78 G. H. Zschornack, *Handbook of X-Ray Data*, Springer, New York, 2007.